

Topological enhancement of a \mathcal{PT} -symmetric Su-Schrieffer-Heeger quantum battery

A-Long Zhou, Ya-Wen Xiao, Nuo Xu, Li-Li Gao, Long-Jie Li, Hang Zhou, Zi-Min Li,* and Chuan-Cun Shu†

Institute of Quantum Physics, Hunan Key Laboratory of Nanophotonics and Devices,

Hunan Key Laboratory of Super-Microstructure and Ultrafast Process,

School of Physics, Central South University, Changsha 410083, China

(Dated: November 18, 2025)

We investigate a non-Hermitian quantum battery based on the Su-Schrieffer-Heeger (SSH) lattice, charged through a \mathcal{PT} -symmetric protocol that alternates gain and loss between the two sublattices. The interplay between lattice topology and non-Hermiticity gives rise to both bulk and edge exceptional points (EPs), which govern the charging dynamics. In the topological regime, an edge-state EP emerges at an exponentially small non-Hermitian strength, resulting in early \mathcal{PT} -symmetry breaking and rapid energy accumulation. This topological enhancement originates from the \mathcal{PT} -symmetric non-Hermitian dynamics, in which the broken-symmetry edge mode with the largest imaginary part of the eigenvalue dominates the time evolution. Consequently, the topological phase consistently yields higher stored energy and faster saturation than the trivial configuration across all parameter regimes and system sizes. These findings demonstrate that topology constitutes a genuine physical resource for enhancing the performance of quantum batteries.

I. INTRODUCTION

Quantum batteries (QBs) are quantum systems that store and deliver energy by exploiting inherently quantum resources such as coherence, entanglement and collective interactions [1–9]. They have become an active research topic at the interface of quantum information and thermodynamics. Various QB models have demonstrated advantages in charging power, efficiency, and robustness over classical counterparts. For example, collective charging schemes in Dicke or Tavis–Cummings models show how cooperative quantum effects can increase power beyond the linear scaling of independent units [10–17]. Nevertheless, identifying additional physical mechanisms that can enhance charging speed or stability under realistic conditions remains a central challenge in the development of practical quantum batteries [9, 18].

Beyond quantum correlations, topological phases of matter offer an alternative approach to controlling energy storage and transfer. Their global invariants protect edge states and yield robust phase transitions, suggesting that topological features could enhance the stability and efficiency of quantum-battery performance [19, 20]. Among the simplest one-dimensional realizations is the Su–Schrieffer–Heeger (SSH) model, a dimerized lattice with alternating couplings that serves as a minimal platform for exploring topology in charging dynamics [21].

Recent studies have begun to explore the SSH model in the context of energy storage. For instance, Ref. [22] considered a spin-chain QB with SSH-type couplings and examined how a quantum phase transition influences the charging performance, but without analyzing the explicit role of topology. More recently, Ref. [23] introduced the concept of topological quantum batteries and showed

that, in open systems, non-trivial topological phases support bound states that suppress dissipation and allow the system to maintain stored energy over long times. Building on these studies, we examine the SSH lattice itself as a quantum battery, emphasizing how topological phases modify charging efficiency and stability.

While many QB proposals assume isolated unitary dynamics, in practice no quantum system is completely free from environmental effects. Dissipation and decoherence play an inevitable role and must therefore be incorporated into realistic models of QBs [2, 24–30]. A standard theoretical framework for describing such open-system effects is the Lindblad master equation, which enables the treatment of non-unitary evolution in a controlled manner [31, 32]. In certain regimes, however, these open dynamics can be effectively captured by non-Hermitian Hamiltonians, leading to simplified yet insightful descriptions [33–35]. Recent studies have shown that non-Hermitian dynamics can themselves enhance the performance of quantum batteries [36]. By engineering gain and loss, one can achieve faster charging or more robust energy storage compared with purely Hermitian setups. A particularly intriguing case is that of parity-time (\mathcal{PT}) symmetric Hamiltonians, which balance gain and loss in a way that preserves real spectra in certain regimes [37–40]. The role of \mathcal{PT} symmetry in quantum batteries remains largely unexplored. It is therefore natural to ask how \mathcal{PT} -symmetric extensions of the SSH model may compete or cooperate with topological effects in determining charging performance.

From an experimental perspective, the key ingredients of non-Hermitian and topological lattice models have already been realized in several platforms. Photonic lattices and coupled-resonator arrays can implement SSH-type band structures with tunable gain and loss, enabling direct access to \mathcal{PT} symmetry and exceptional-point physics [33, 41, 42]. In addition, cavity- and circuit-QED architectures provide versatile settings in which driven light-matter interactions realize general-

* zimin.li@csu.edu.cn

† cc.shu@csu.edu.cn

ized quantum Rabi and lattice models with effective non-Hermitian and topological features [43–50]. These developments indicate that the \mathcal{PT} -symmetric topological mechanisms explored here could be transplanted into cavity-based quantum-battery charging schemes, where an SSH-type battery is coupled to structured photonic modes in a controllable way.

In this work, we investigate a \mathcal{PT} -symmetric SSH quantum battery that integrates topological and non-Hermitian effects. The interplay between topology and \mathcal{PT} symmetry gives rise to both bulk and edge exceptional points (EPs), which determine the charging dynamics. Our analysis reveals that the edge EP, appearing only in the topological phase, triggers early symmetry breaking and enables faster and more complete energy accumulation. These results highlight the cooperative role of topology and non-Hermiticity in optimizing the performance of quantum batteries.

II. SU–SCHRIEFFER–HEEGER (SSH) QUANTUM BATTERY

A. SSH model and chiral symmetry

We consider a one-dimensional dimerized chain of $2N$ sites arranged in N unit cells, each containing an A and a B sublattice site. The SSH Hamiltonian is given by

$$H_{\text{SSH}} = \sum_{n=1}^N \left[J_1 a_n^\dagger b_n + J_2 b_n^\dagger a_{n+1} + H.c. \right], \quad (1)$$

where a_n and b_n annihilate excitations on sublattices A and B of cell n , respectively, and $J_{1(2)} \geq 0$ denote the intra-(inter-)cell couplings.

The model possesses chiral (sublattice) symmetry generated by

$$\Gamma = \sum_n (a_n^\dagger a_n - b_n^\dagger b_n), \quad (2)$$

which anticommutes with H_{SSH} , $\{\Gamma, H_{\text{SSH}}\} = 0$ and therefore ensures that the spectrum is symmetric about zero energy ($E \leftrightarrow -E$), see Appendix A for further discussion.

Under periodic boundary conditions and Bloch transformation $a_k^\dagger = N^{-1/2} \sum_n e^{ikn} a_n^\dagger$ and $b_k^\dagger = N^{-1/2} \sum_n e^{ikn} b_n^\dagger$, the Bloch Hamiltonian becomes

$$h(k) = \begin{pmatrix} 0 & J_1 + J_2 e^{-ik} \\ J_1 + J_2 e^{ik} & 0 \end{pmatrix}, \quad (3)$$

whose bulk spectrum

$$E_{\text{SSH}}(k) = \pm \sqrt{J_1^2 + J_2^2 + 2J_1 J_2 \cos k} \quad (4)$$

closes its gap at $J_1 = J_2$, which marks the topological transition. For open boundaries, the chain hosts zero-energy edge states when $J_1 < J_2$, corresponding to a

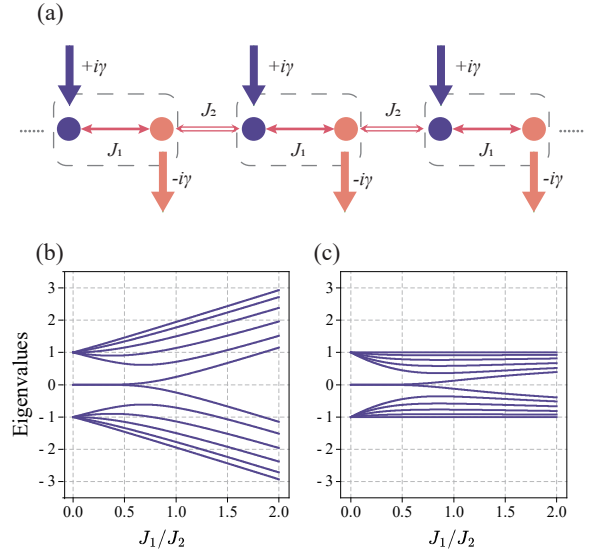


FIG. 1. (a) SSH lattice with alternating couplings J_1 and J_2 , serving as the basis for the \mathcal{PT} -symmetric SSH model with balanced gain and loss γ . (b) Bulk energy spectrum of the Hermitian SSH model. (c) Normalized energy spectrum, used to eliminate the trivial dependence on the overall energy scale and to enable consistent evaluation of charging performance.

dimerization centered on the weaker bonds, while it becomes topologically trivial for $J_1 > J_2$.

The SSH lattice configuration is sketched in Fig. 1(a), which also forms the basis for the \mathcal{PT} -symmetric extension introduced in Sec. II B. Figure 1(b) shows the corresponding bulk energy spectrum of the Hermitian SSH model, while the normalized spectrum in Fig. 1(c) will be discussed later in Sec. II C. All the figures are generated with $N = 6$.

B. \mathcal{PT} -symmetric SSH model

We now consider a charging scheme with balanced gain and loss on the two sublattices, effectively described by a \mathcal{PT} -symmetric extension of the SSH lattice introduced above. The corresponding non-Hermitian Hamiltonian is

$$H_{\mathcal{PT}} = H_{\text{SSH}} + i\gamma \sum_{n=1}^N (a_n^\dagger a_n - b_n^\dagger b_n) \equiv H_{\text{SSH}} + i\gamma \Gamma, \quad (5)$$

where $\gamma > 0$ quantifies the strength of the gain–loss coupling [51]. The Hamiltonian commutes with the combined \mathcal{PT} operator, where \mathcal{P} exchanges the sublattices and \mathcal{T} denotes complex conjugation. This ensures a real spectrum in the unbroken \mathcal{PT} -symmetric regime. The effective non-Hermitian Hamiltonian can be derived from the Lindblad master equation by neglecting the quantum-jump terms, as detailed in Appendix B.

Under periodic boundary conditions, the bulk disper-

TABLE I. Classification of topological phases and \mathcal{PT} -symmetric regimes of the SSH model.

	$0 < \gamma < \gamma_e$	$\gamma_e < \gamma < J_1 - J_2 $	$ J_1 - J_2 < \gamma < J_1 + J_2 $	$\gamma > J_1 + J_2 $
$J_1 > J_2$ (Trivial)	Unbroken	Unbroken	Partially broken	Fully broken
$J_1 < J_2$ (Topological)	Unbroken	Edge-broken	Bulk-partially broken	Fully broken

sion in momentum space reads

$$E_{\mathcal{PT}}(k) = \pm \sqrt{J_1^2 + J_2^2 + 2J_1 J_2 \cos k - \gamma^2}. \quad (6)$$

The EPs occur at $\gamma = |J_1 \pm J_2|$, where pairs of eigenvalues coalesce and the energy spectrum changes from real to complex, marking the spontaneous breaking of \mathcal{PT} symmetry. These EPs separate three \mathcal{PT} -symmetric regimes: unbroken ($\gamma < |J_1 - J_2|$), partially broken ($|J_1 - J_2| < \gamma < |J_1 + J_2|$), and fully broken ($\gamma > |J_1 + J_2|$). For open boundary conditions, the hybridized edge pair experiences an additional EP at

$$\gamma_e = J_1 \frac{1 - (J_1/J_2)^2}{1 - (J_1/J_2)^{2N}} (J_1/J_2)^{N-1}, \quad (7)$$

which decreases exponentially with the system size N and vanishes in the trivial phase [51]. This edge EP originates from the coalescence of the two midgap edge modes and is a unique signature of the topological regime.

Figures 2(a)-2(d) show the real and imaginary parts of the spectrum as functions of gain-loss strength γ for topological ($J_1/J_2 = 0.5$) and trivial ($J_1/J_2 = 1.5$) phases. For small γ , all eigenvalues are real, corresponding to the unbroken \mathcal{PT} phase. As γ increases, pairs of eigenvalues coalesce and split into complex-conjugate partners at the EPs, signaling the spontaneous breaking of \mathcal{PT} symmetry. Beyond each EP, one hybridized mode amplifies while its partner decays, reflecting the non-unitary nature of the dynamics.

Bulk EPs appear for $|J_1 - J_2| < \gamma < |J_1 + J_2|$, and the two boundaries $\gamma = |J_1 \pm J_2|$ separate the unbroken, partially broken, and fully broken \mathcal{PT} regimes (vertical dashed lines in Figs. 2(a)-2(d)). In the topological configuration ($J_1 < J_2$), an additional edge EP given by Eq. (7) breaks the \mathcal{PT} symmetry more readily, providing the basis for its enhanced charging performance. The corresponding classification of topological phases and \mathcal{PT} -symmetric regimes is summarized in Table I. Figure 2(e) presents the resulting phase diagram, where the regions are divided according to the boundaries listed in Table I and the topological and \mathcal{PT} regimes are displayed jointly.

C. Non-Hermitian dynamics and performance metrics

The non-Hermitian Hamiltonian $H_{\mathcal{PT}}$ acts as the charger driving the SSH battery. Within the effective-Hamiltonian description, the normalized density matrix

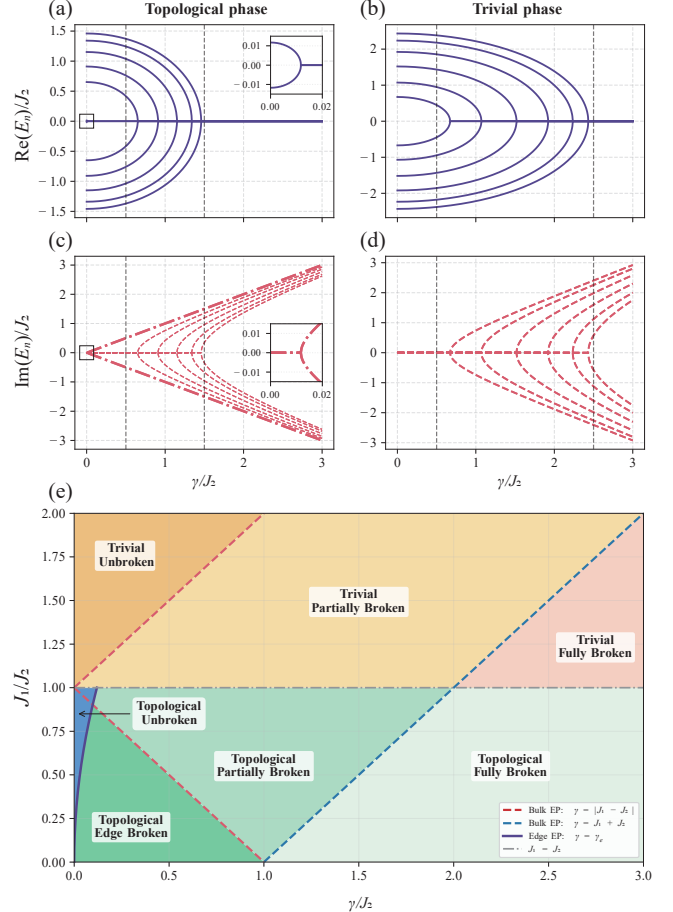


FIG. 2. Spectral structure and phase diagram of the \mathcal{PT} -symmetric SSH model. (a,c) Real and imaginary parts of the eigenvalues in the topological phase ($J_1/J_2 = 0.5$); (b,d) corresponding spectra in the trivial phase ($J_1/J_2 = 1.5$). (e) Phase diagram in the γ - J_1 plane, showing unbroken, partially broken, and fully broken regimes. Dashed lines mark bulk thresholds $\gamma = |J_1 \pm J_2|$ and the solid curve the edge EP $\gamma = \gamma_e$. The figures are generated with $N = 6$.

evolves as [36]

$$\rho(t) = \frac{e^{-iH_{\mathcal{PT}}t} \rho(0) e^{iH_{\mathcal{PT}}^\dagger t}}{\text{Tr}[e^{-iH_{\mathcal{PT}}t} \rho(0) e^{iH_{\mathcal{PT}}^\dagger t}]}, \quad (8)$$

where the initial density matrix $\rho(0)$ is taken as the ground-state projector of H_{SSH} .

Conventionally, the charging energy, average power, and extractable work (ergotropy) are the key quantities used to characterize quantum-battery performance. In

our system, however, since the dynamics is oscillatory and can become non-stationary in the \mathcal{PT} -broken regime, time-averaged power is not a meaningful figure of merit. Moreover, for a battery initialized in the ground state and with work extraction restricted to unitaries, the ergotropy $\mathcal{W}(t)$ effectively coincides with $\Delta E(t)$, as shown in Appendix C. We therefore focus on the stored energy $\Delta E(t)$, defined by

$$\Delta E(t) = E_B(t) - E_B(0), \quad E_B(t) = \text{Tr}[H_B \rho(t)]. \quad (9)$$

To enable consistent comparison across parameters, we remove trivial spectral dilation by normalizing the battery Hamiltonian [28, 36, 52, 53],

$$H_B^{(\text{norm})} = \frac{2H_B - (E_{\max} + E_{\min})\mathbb{I}}{E_{\max} - E_{\min}}, \quad (10)$$

which confines the spectrum to the interval $[-1, 1]$. This rescaling ensures that performance enhancements originate solely from intrinsic topological effects rather than from artificial spectral scaling.

III. CHARGING PERFORMANCE ANALYSIS

A. Charging dynamics in different regimes

Having established the dynamical model and the performance metric, we now turn to the dynamical behavior of the quantum battery, focusing on the time evolution of the stored energy $\Delta E(t)$ under different non-Hermitian parameters γ and topological configurations.

Figures 3(a) and 3(b) show the global evolution of $\Delta E(t)$ for the topological ($J_1/J_2 = 0.5$) and trivial ($J_1/J_2 = 1.5$) phases, respectively. The color scale represents the normalized energy $\Delta E(t)$ as a function of both non-Hermitian parameter γ and time. Three distinct dynamical regimes emerge, corresponding to the unbroken, partially broken, and fully broken \mathcal{PT} phases identified in Fig. 2. In the unbroken phase, all eigenvalues remain real and the system exhibits persistent oscillations in $\Delta E(t)$, forming long-lived ripples in the time domain. In the partially broken phase, the system first displays oscillations and then saturates, leading to a mixed region characterized by a transient oscillatory pattern followed by a steady plateau. In the fully broken phase, all eigenvalues are complex and $\Delta E(t)$ increases monotonically to its saturation value without oscillations.

Comparing Figs. 3(a) and 3(b), the topological phase exhibits a broader region of partial \mathcal{PT} breaking due to the presence of edge states, whereas the trivial phase experiences symmetry breaking only through bulk modes. As a result, the topological phase maintains an energetic advantage across all γ values, consistent with the earlier phase diagram. This asymmetry can be intuitively understood as a “selective breaking” process: the edge-state EP γ_e enables early activation of non-Hermitian

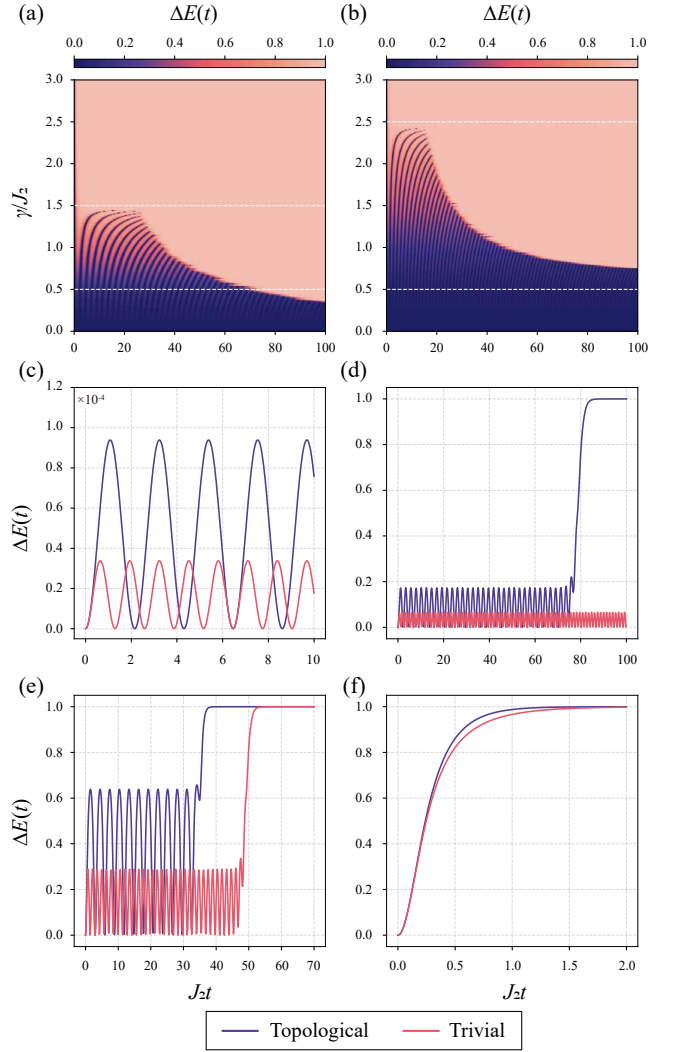


FIG. 3. Time evolution of the stored energy $\Delta E(t)$ under different non-Hermitian parameters γ and topological configurations. (a,b) Global maps of $\Delta E(t)$ for the topological ($J_1/J_2 = 0.5$) and trivial ($J_1/J_2 = 1.5$) phases, respectively. (c)–(f) Representative traces of $\Delta E(t)$ at $\gamma/J_2 = 0.01, 0.45, 1.0$, and 2.8 , corresponding to the unbroken, edge-state broken, partially broken, and fully broken \mathcal{PT} regimes. Purple and red curves denote the topological and trivial phases, respectively. The topological phase exhibits faster energy growth and earlier saturation across all γ values.

gain in the topological case, while the trivial system requires stronger γ to reach comparable dynamics.

Figures 3(c)–3(f) illustrate representative time traces of $\Delta E(t)$ for four specific γ values, corresponding to the unbroken, edge-broken, partially broken, and fully broken \mathcal{PT} regimes.

At $\gamma/J_2 = 0.01$ [Fig. 3(c)], both phases lie in the unbroken regime, where all eigenvalues remain real and the dynamics is purely oscillatory. The stored energy exhibits sustained periodic oscillations with small amplitude, reflecting coherent population exchange between

the lattice sites. In this limit, the charging behavior of the topological and trivial batteries is nearly identical, and no advantage is observed.

When γ/J_2 increases to 0.45 [Fig. 3(d)], the trivial phase remains unbroken, whereas the topological phase undergoes edge-state \mathcal{PT} breaking. The non-Hermitian growth of the broken edge mode amplifies its population, rapidly transferring energy into the battery sublattice. Consequently, the topological battery shows a sharp rise in $\Delta E(t)$ followed by a slow saturation toward a high steady value, while the trivial system continues to oscillate around a much lower mean energy. This edge-driven amplification marks the regime where the topological advantage is most pronounced.

Upon further increase to $\gamma/J_2 = 1.0$ [Fig. 3(e)], both phases enter the bulk partially broken regime, in which real and complex eigenmodes coexist. The early-time oscillations originate from the remaining real spectrum, while the long-time approach to saturation is governed by the dominance of complex-conjugate pairs leading to non-unitary amplification and decay. Although the overall charging efficiency begins to level off, the topological configuration still achieves faster convergence.

In the fully broken regime ($\gamma/J_2 = 2.8$) [Fig. 3(f)], all eigenvalues become complex and the charging process becomes monotonic. The stored energy $\Delta E(t)$ increases steadily toward its maximum attainable value. Even under such strong non-Hermiticity, the topological battery retains a slight speed advantage, completing the charge more rapidly and stabilizing earlier than the trivial counterpart.

Overall, the results reveal that the topological phase consistently outperforms the trivial one across all non-Hermitian regimes. This advantage originates from the extended partial-breaking region of the topological phase, enabled by the early edge-state EP, which allows faster and more complete energy accumulation.

B. Quantitative measures of charging performance

To confirm whether the dynamical behaviors identified above persist across the full parameter space, we introduce two performance indicators extracted directly from the time evolution of $\Delta E(t)$. These indicators characterize complementary aspects of short- and long-time charging behavior and allow us to evaluate the robustness of the topological advantage under varying non-Hermitian strength γ and coupling ratio J_1/J_2 .

The first quantity is the amplitude of the first energy peak, denoted $\Delta E_{\text{peak}}^{(1)}$. This peak arises from the coherent population transfer that dominates the early-time oscillatory regime and therefore measures the battery's initial responsiveness to the non-Hermitian drive. A larger value of $\Delta E_{\text{peak}}^{(1)}$ indicates more efficient short-time energy absorption and provides a meaningful comparison even in regions where long-time saturation does not occur.

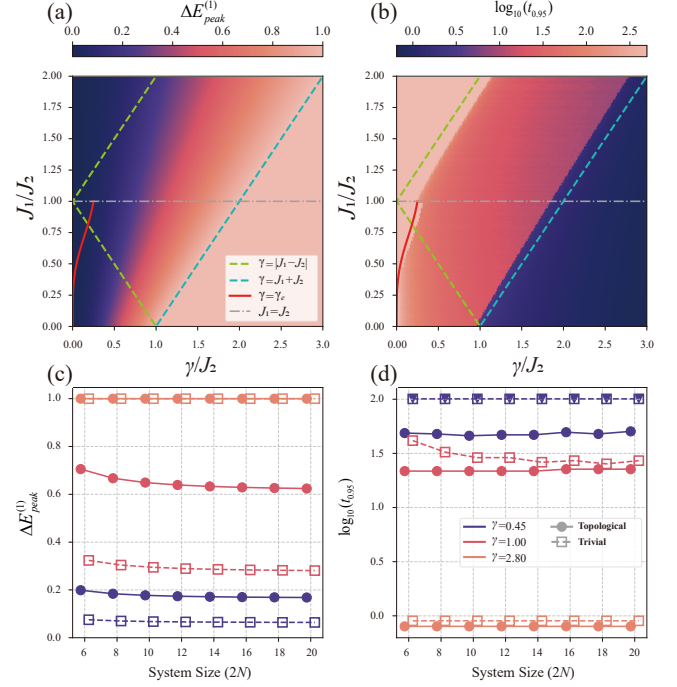


FIG. 4. Dependence of the charging performance on system parameters of the \mathcal{PT} -symmetric SSH quantum battery. (a) Amplitude of the first energy peak $\Delta E_{\text{peak}}^{(1)}$ in the γ - J_1 plane. (b) Logarithmic saturation time $\log_{10}(t_{0.95})$ in the same parameter space. The phase boundaries $J_1 = J_2$ and the \mathcal{PT} -symmetry-breaking thresholds γ_e , $|J_1 - J_2|$, and $J_1 + J_2$ are indicated for reference. (c) System-size dependence of $\Delta E_{\text{peak}}^{(1)}$ for three representative values of the gain-loss strength $\gamma/J_2 = 0.45$, 1.0, and 2.8. (d) Corresponding system-size dependence of the saturation time, shown as $\log_{10}(t_{0.95})$. In panels (c) and (d), solid curves correspond to the topological configuration ($J_1/J_2 = 0.5$) and dashed curves correspond to the trivial configuration ($J_1/J_2 = 1.5$).

The second quantity is the saturation time $t_{0.95}$, defined as the earliest time at which the stored energy reaches 95% of its long-time asymptotic value. This timescale captures how quickly non-unitary amplification and dissipation drive the system toward its steady charging plateau, serving as a natural measure of long-time charging speed.

Together, $\Delta E_{\text{peak}}^{(1)}$ and $t_{0.95}$ provide a comprehensive characterization of transient and steady-state behavior, enabling us to verify the generality of the charging trends observed in Sec. III A across the entire γ - J_1 parameter plane. In fully oscillatory regimes where the battery never saturates, $t_{0.95}$ is effectively infinite, whereas in monotonic regimes $\Delta E_{\text{peak}}^{(1)}$ is set to unity. Since $t_{0.95}$ spans several orders of magnitude in the partially and fully broken regimes, we present $\log_{10}(t_{0.95})$ for clarity.

Figures 4(a) and 4(b) display these two metrics in the γ - J_1 plane. Panel (a) shows the distribution of the first energy peak $\Delta E_{\text{peak}}^{(1)}$, while panel (b) presents the loga-

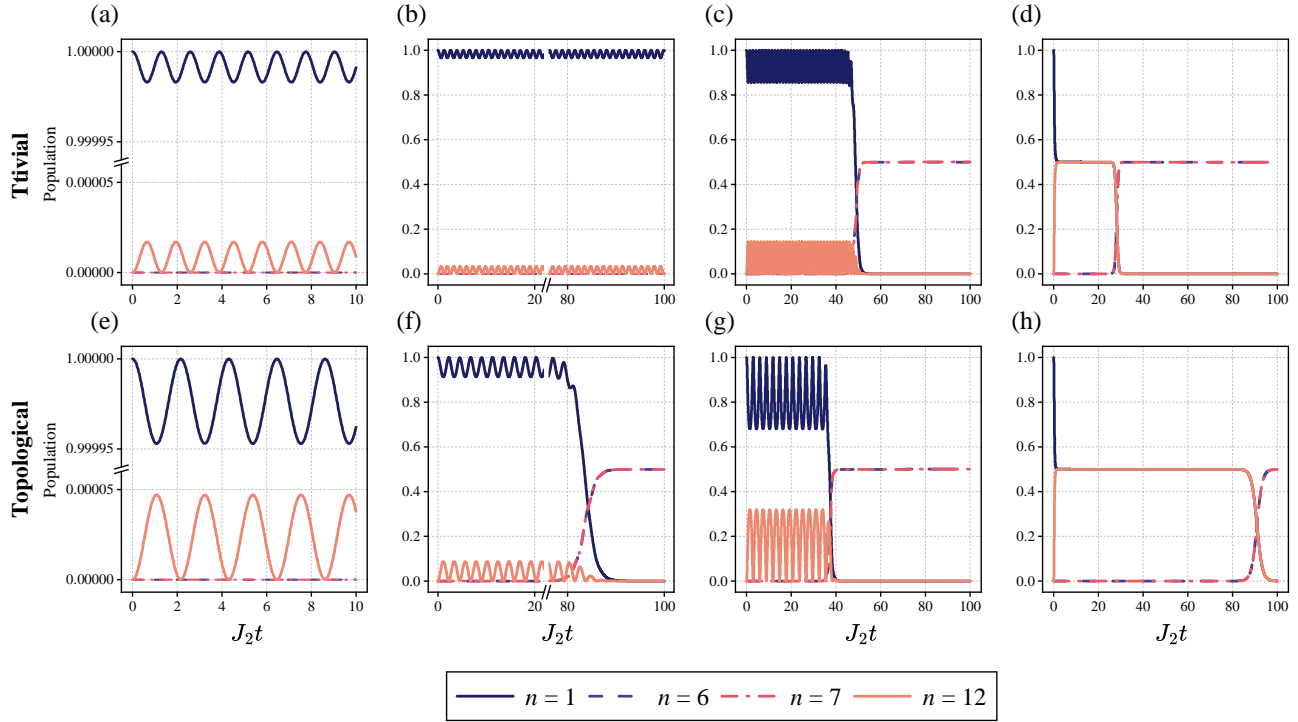


FIG. 5. Time-dependent populations of selected eigenstates ϕ_n of the SSH battery during \mathcal{PT} -symmetric charging. (a,e) Unbroken regime ($\gamma/J_2 = 0.01$); (b,f) edge-state broken regime ($\gamma/J_2 = 0.45$); (c,g) partially broken regime ($\gamma/J_2 = 1.0$); (d,h) fully broken regime ($\gamma/J_2 = 2.8$). Left and right panels correspond to the topological and trivial phases, respectively. The dominance of edge-related midgap states after the edge EP and the late-time flow toward central bulk modes in the fully broken regime are both consistent with growth-rate selection by $\text{Im } E$.

rithmic saturation time $\log_{10}(t_{0.95})$. Both maps include the boundaries of the topological transition ($J_1 = J_2$) and the \mathcal{PT} -symmetry-breaking thresholds γ_e , $|J_1 - J_2|$, and $J_1 + J_2$. Across all regions, the topological phase exhibits larger $\Delta E_{\text{peak}}^{(1)}$ and shorter $t_{0.95}$ than the trivial phase, indicating uniformly superior performance.

This enhancement originates from the early edge-state EP γ_e , which occurs at a much smaller non-Hermitian strength than the bulk thresholds. As a result, the topological system enters the partially broken regime at significantly weaker gain-loss coupling, allowing non-unitary amplification to take effect earlier. The contrast between the regions just below and above γ_e highlights the crucial role of early \mathcal{PT} -symmetry breaking as the mechanism enabling efficient charging.

Since the position of the edge-state EP depends exponentially on system size, we next investigate how the performance scales with the total number of sites $2N$. Figures 4(c) and 4(d) show the system-size dependence of $\Delta E_{\text{peak}}^{(1)}$ and $\log_{10}(t_{0.95})$, respectively, for three representative non-Hermitian strengths $\gamma/J_2 = 0.45$, 1.0, and 2.8. In all cases, the curves for the topological and trivial configurations are clearly separated: the topological battery reaches a higher first-peak energy and a shorter saturation time than the trivial one for all three values of γ/J_2 . This confirms that the topological enhancement of

both transient and long-time performance is not a finite-size artifact, but persists as the system size increases.

At $\gamma/J_2 = 0.45$, the difference is particularly pronounced. The topological system enters the edge-broken regime and achieves saturation, whereas the trivial system remains unbroken and fails to saturate, demonstrating a qualitative distinction in their dynamical behavior. As the system size increases, the critical value γ_e decreases, effectively expanding the edge-broken region in the $\gamma-J_1$ plane and further amplifying the topological advantage.

Overall, these quantitative metrics confirm that topological edge states substantially enhance both the transient and long-term charging characteristics of the \mathcal{PT} -symmetric SSH quantum battery.

C. Microscopic mechanism of the charging dynamics

To uncover the microscopic origin of the charging behavior, we examine the time-dependent populations of the eigenstates of the SSH battery Hamiltonian during the evolution under the non-Hermitian charger. We denote by ϕ_1 and ϕ_{2N} the lowest- and highest-energy eigenstates of H_{SSH} , respectively, and label the remaining eigenstates $\{\phi_j\}_{j=2}^{2N-1}$ in increasing energy order. Because

$\{\Gamma, H_{\text{SSH}}\} = 0$, the spectrum of H_{SSH} forms $\pm E_j$ pairs, and the drive term $i\gamma\Gamma$ couples each $+E_j$ state predominantly to its $-E_j$ partner. This produces an effective two-level exchange in the weakly non-Hermitian regime.

The population dynamics across different values of γ can be interpreted using the universal principles of non-Hermitian evolution summarized in Appendix D. Early-time behavior is controlled by the initial projections onto the eigenmodes, intermediate-time behavior by the gap between the leading imaginary parts, and long-time behavior by the mode with the largest imaginary part.

In the unbroken \mathcal{PT} regime ($\gamma/J_2 = 0.01$), all eigenvalues are real and the chiral selection rule confines the dynamics essentially to the extremal pair (ϕ_1, ϕ_{2N}) . Both phases therefore display small-amplitude, long-lived oscillations, as seen in Figs. 5(a) and 5(e). In a simple two-level approximation within this extremal subspace, the non-Hermitian drive $i\gamma\Gamma$ generates an off-diagonal coupling $\Gamma_{2N,1} = \langle \phi_{2N} | \Gamma | \phi_1 \rangle$, and the maximal population transferred to ϕ_{2N} scales as $P_{2N}^{(\text{max})} \propto (2\gamma|\Gamma_{2N,1}|/\Delta E)^2$, with $\Delta E = E_{2N} - E_1$. Thus, the oscillation amplitude is set by the ratio $|\Gamma_{2N,1}|/|\Delta E|$, which can be confirmed numerically by comparing the topological and trivial configurations. The same mechanism also underlies the systematically larger early-time oscillation amplitudes of the topological chain at higher gain-loss strengths, as seen by comparing Figs. 5(f) and 5(g) with Figs. 5(b) and 5(c).

At $\gamma/J_2 = 0.45$, the two phases separate due to the distinct fates of the edge doublet. In the topological chain, the edge modes encounter the EP at the exponentially small threshold γ_e , causing one edge superposition to acquire a positive imaginary part and grow exponentially. After normalization, this amplifying component rapidly dominates the population, leading to the takeover of the midgap states (ϕ_6, ϕ_7) as shown in Fig. 5(f). The trivial chain lacks edge modes and remains unbroken at this γ , displaying only weak oscillations as in Fig. 5(b).

When $\gamma/J_2 = 1.0$, both systems enter the bulk partially broken regime and possess a mixture of real and complex eigenvalues. The short-time dynamics is still governed by oscillatory exchange among modes with real eigenvalues, whereas the long-time dynamics is dictated by the modes with the largest imaginary parts. Because the topological chain broke its edge pair at $\gamma_e \ll |J_1 - J_2|$, population is funneled into the amplifying subspace earlier than in the trivial chain. This head start produces the faster saturation visible in Figs. 5(c) and 5(g).

In the fully broken regime ($\gamma/J_2 = 2.8$), all eigenvalues are complex and appear in conjugate pairs with opposite imaginary parts. Modes with positive imaginary parts are exponentially amplified, while their partners with negative imaginary parts are suppressed, and the normalized dynamics at late times is therefore governed by the former. For the parameters used in Fig. 5, the largest imaginary parts are carried by modes near the band center, so both chains ultimately converge to the (ϕ_6, ϕ_7) . Within each broken pair, the non-Hermitian drive combines exponential amplification and decay with coherent

coupling, leading to a transient oscillatory exchange of population before the amplifying component prevails. As a result, $\Delta E(t)$ exhibits an almost monotonic increase toward its saturation value in both phases. However, the approach to this limit still differs between the two configurations: in the trivial chain the gap between the two leading imaginary parts is larger, so the band-center pair overtakes competing modes more quickly, whereas in the topological chain several modes with comparable imaginary parts compete for longer times, delaying the emergence of the (ϕ_6, ϕ_7) plateau.

In summary, the charging dynamics is governed by the interplay between chiral-selection-induced couplings, initial projections, and the hierarchy of imaginary parts of the eigenvalues. These factors explain the qualitative differences between the trivial and topological configurations across all non-Hermitian regimes and identify the edge-state EP as the microscopic origin of the enhanced charging speed in the topological phase.

IV. CONCLUSIONS

In this work, we have studied the \mathcal{PT} -symmetric Su-Schrieffer-Heeger (SSH) model as a prototype of a non-Hermitian quantum battery. The coexistence of topology and balanced gain-loss gives rise to both bulk and edge exceptional points (EPs), which organize the charging dynamics across different non-Hermitian regimes.

An edge-state EP, present only in the topological phase, occurs at a much smaller non-Hermitian strength γ_e than the bulk thresholds and triggers early \mathcal{PT} -symmetry breaking. This early onset produces a broad edge-broken region in the phase diagram and enables faster and more complete charging compared with the trivial phase.

Quantitative analysis of the stored energy $\Delta E(t)$ and its derived metrics, the first-peak amplitude and the saturation time, confirms that the topological configuration consistently achieves higher transient energy and quicker saturation across all parameter ranges and system sizes. Microscopic population dynamics show that, once the edge mode is broken, the eigenstate with the largest imaginary part of the eigenvalue eventually dominates the evolution, providing a direct mechanism for accelerated accumulation of energy.

These results demonstrate that topology and non-Hermiticity can act cooperatively to enhance quantum energy storage, offering a viable route toward designing high-performance quantum batteries based on non-Hermitian control. Future extensions may explore interacting or many-body realizations, where collective charging and dissipation could yield new scaling behaviors. Possible experimental implementations in photonic lattices, superconducting circuits, or cold-atom arrays would enable direct tests of the predicted edge-induced enhancement and probe the robustness of topological advantages in non-Hermitian quantum devices.

ACKNOWLEDGMENTS

This work was supported by the National Natural Science Foundation of China (Grant No. 12205383, 12274470) and the Hunan Provincial Natural Science Foundation (Grant No. 2024JJ6483). A.-L. Zhou was also supported by the Fundamental Research Funds for the Central Universities of Central South University under Grant No.1053320214335.

Appendix A: Chiral symmetry and transition matrix elements

In this appendix, we clarify how the chiral symmetry of the Hermitian SSH Hamiltonian constrains its spectrum and the matrix elements of the sublattice operator Γ , and how these constraints underlie the selection rules used in the main text.

We recall that the SSH Hamiltonian H_{SSH} introduced in Eq. (1) acts on a chain of N unit cells with sublattice operators a_n and b_n . The sublattice (chiral) operator is defined as

$$\Gamma = \sum_{n=1}^N (a_n^\dagger a_n - b_n^\dagger b_n). \quad (\text{A1})$$

A straightforward calculation shows that

$$\{\Gamma, H_{\text{SSH}}\} = \Gamma H_{\text{SSH}} + H_{\text{SSH}}\Gamma = 0, \quad (\text{A2})$$

so H_{SSH} possesses an exact chiral symmetry.

Let $|\phi_j\rangle$ be the normalized eigenstates of H_{SSH} , ordered so that $H_{\text{SSH}}|\phi_j\rangle = E_j|\phi_j\rangle$ with $E_1 \leq E_2 \leq \dots \leq E_{2N}$. Using $\{\Gamma, H_{\text{SSH}}\} = 0$, we obtain

$$\begin{aligned} 0 &= \langle\phi_m|\{\Gamma, H_{\text{SSH}}\}|\phi_n\rangle \\ &= (E_m + E_n) \langle\phi_m|\Gamma|\phi_n\rangle. \end{aligned} \quad (\text{A3})$$

For nondegenerate eigenvalues, this implies the “chiral selection rule”

$$(E_m + E_n) \neq 0 \Rightarrow \langle\phi_m|\Gamma|\phi_n\rangle = 0. \quad (\text{A4})$$

In other words, the sublattice operator Γ only couples eigenstates whose energies are opposite, $E_m = -E_n$. This condition is a direct consequence of chiral symmetry and does not depend on microscopic details.

Because the SSH spectrum is symmetric around zero energy, we can pair the eigenstates as $(|\phi_j\rangle, |\phi_{\bar{j}}\rangle)$ with $E_{\bar{j}} = -E_j$. For an open chain of $2N$ sites it is convenient to choose the ordering such that $\bar{j} = 2N + 1 - j$, so that $(|\phi_1\rangle, |\phi_{2N}\rangle)$, $(|\phi_2\rangle, |\phi_{2N-1}\rangle)$, and so on form chiral partner pairs. Within this convention, the matrix elements of Γ in the energy eigenbasis,

$$M_{mn} = \langle\phi_m|\Gamma|\phi_n\rangle, \quad (\text{A5})$$

are strongly concentrated near the anti-diagonal $m = \bar{n}$, while elements with $m \neq \bar{n}$ are suppressed by the selection rule.

For the finite-size parameters used in the main text, we have verified numerically that the largest matrix element is

$$|M_{1,2N}| = |\langle\phi_1|\Gamma|\phi_{2N}\rangle| \simeq 1, \quad (\text{A6})$$

whereas $M_{1,2}$, $M_{1,3}$, and other off-pair terms are typically at least an order of magnitude smaller. Similar behavior is found for other chiral pairs $(\phi_j, \phi_{\bar{j}})$. This pattern implies that, in the weakly non-Hermitian regime where the drive term $i\gamma\Gamma$ acts as a perturbation, the dominant transition channel induced by Γ connects the lowest- and highest-energy eigenstates, while additional couplings within the same energy sign are strongly suppressed.

In the presence of the non-Hermitian gain-loss term, the full \mathcal{PT} -symmetric Hamiltonian

$$H_{\mathcal{PT}} = H_{\text{SSH}} + i\gamma\Gamma \quad (\text{A7})$$

no longer anticommutes with Γ . Indeed,

$$\{\Gamma, H_{\mathcal{PT}}\} = 2i\gamma\mathbb{I} \neq 0. \quad (\text{A8})$$

The chiral symmetry is thus explicitly broken once $\gamma \neq 0$. Nevertheless, the matrix structure of Γ in the $\{|\phi_j\rangle\}$ basis retains its pronounced anti-diagonal character, and the extremal pair (ϕ_1, ϕ_{2N}) continues to play a special role. This *spectral memory* explains why, even when non-Hermiticity is present, the early-time charging dynamics is dominated by transitions between the lowest- and highest-energy eigenstates, as discussed in Sec. III C.

Appendix B: Effective \mathcal{PT} -symmetric SSH Hamiltonian from a Lindblad master equation

In this appendix, we show how the non-Hermitian \mathcal{PT} -symmetric SSH Hamiltonian used in the main text can be obtained as an effective description of a Lindblad master equation with balanced gain and loss on the two sublattices.

We start from the standard Gorini–Kossakowski–Sudarshan–Lindblad master equation

$$\dot{\rho} = -i[H_{\text{SSH}}, \rho] + \sum_{\mu} \left(L_{\mu}\rho L_{\mu}^\dagger - \frac{1}{2}\{L_{\mu}^\dagger L_{\mu}, \rho\} \right), \quad (\text{B1})$$

where H_{SSH} is the Hermitian SSH Hamiltonian defined in Eq. (1) and $\{L_{\mu}\}$ are the jump operators describing incoherent processes. To model spatially uniform gain on sublattice A and loss on sublattice B we take [54]

$$L_{a,n} = \sqrt{\kappa} a_n^\dagger, \quad L_{b,n} = \sqrt{\kappa} b_n, \quad (\text{B2})$$

with a common bare rate $\kappa > 0$ and $n = 1, \dots, N$ labeling the unit cells. Here $L_{a,n}$ creates a particle on sublattice A at cell n (gain), while $L_{b,n}$ annihilates a particle on sublattice B at cell n (loss).

In the quantum-trajectory picture, the density matrix evolution can be decomposed into deterministic no-jump segments separated by stochastic quantum jumps. Between jumps, the unnormalized state evolves under an effective non-Hermitian Hamiltonian [55–57]

$$H_{\text{eff}} = H_{\text{SSH}} - \frac{i}{2} \sum_{\mu} L_{\mu}^{\dagger} L_{\mu}. \quad (\text{B3})$$

For the gain and loss operators specified above, the non-Hermitian contribution reads

$$\begin{aligned} -\frac{i}{2} \sum_{\mu} L_{\mu}^{\dagger} L_{\mu} &= -\frac{i}{2} \kappa \sum_n (a_n a_n^{\dagger} + b_n^{\dagger} b_n) \\ &= -\frac{i}{2} \kappa \sum_n [1 - a_n^{\dagger} a_n + b_n^{\dagger} b_n]. \end{aligned} \quad (\text{B4})$$

Using the canonical (anti)commutation relation $a_n a_n^{\dagger} = 1 - a_n^{\dagger} a_n$, we obtain

$$\begin{aligned} H_{\text{eff}} &= H_{\text{SSH}} + \frac{i\kappa}{2} \sum_n (a_n^{\dagger} a_n - b_n^{\dagger} b_n) - \frac{i\kappa N}{2} \mathbb{I} \\ &= H_{\text{SSH}} + \frac{i\kappa}{2} \Gamma + \text{const} \times \mathbb{I}, \end{aligned} \quad (\text{B5})$$

where Γ is the sublattice imbalance operator defined in Eq. (2) and the last term is a purely imaginary c-number shift proportional to the identity.

The constant term produces only an overall phase and norm change of the unnormalized state and has no effect on the relative populations in the energy basis or on observable quantities after renormalization. We therefore drop this term and identify the effective non-Hermitian Hamiltonian as

$$H_{\text{eff}} \simeq H_{\text{SSH}} + \frac{i\kappa}{2} \Gamma. \quad (\text{B6})$$

Introducing the gain–loss strength

$$\gamma = \frac{\kappa}{2}, \quad (\text{B7})$$

we recover precisely the \mathcal{PT} -symmetric SSH Hamiltonian used in the main text,

$$H_{\mathcal{PT}} = H_{\text{SSH}} + i\gamma \Gamma. \quad (\text{B8})$$

In the main text, we focus on the deterministic no-jump evolution generated by $H_{\mathcal{PT}}$ and, after renormalization, work with the normalized density matrix given in Eq. (8). Within the quantum-trajectory framework, this corresponds to conditioning on realizations where no quantum jumps are recorded during the charging process. Such an effective non-Hermitian description is widely used when the jump probability is low on the relevant timescales or when post-selection on no-click events is experimentally feasible. In platforms such as photonic lattices, superconducting circuits, and cold-atom setups, post-selected dynamics of this type has been employed to

realize and probe \mathcal{PT} -symmetric Hamiltonians in practice [42, 58, 59].

For real γ , the Hamiltonian $H_{\mathcal{PT}}$ commutes with the combined \mathcal{PT} operator discussed in Sec. II B, leading to real eigenvalues in the unbroken \mathcal{PT} -symmetric regime.

Appendix C: Equivalence between ergotropy and charging energy

For completeness, we provide here a derivation showing that the ergotropy is exactly equal to the stored energy for the charging protocol considered in this work. The ergotropy [8, 60, 61] of a quantum battery is defined as

$$\mathcal{W}(t) = \text{Tr}[H_B \rho(t)] - \min_U \text{Tr}[H_B U \rho(t) U^{\dagger}], \quad (\text{C1})$$

where H_B denotes the battery Hamiltonian and $\rho(t)$ is the density matrix of the battery at time t . The minimum in Eq. (C1) is achieved for the so-called *passive state*,

$$\rho_{\text{p}} = \sum_k r_k^{\downarrow} |\varepsilon_k^{\uparrow}\rangle \langle \varepsilon_k^{\uparrow}|, \quad (\text{C2})$$

where r_k^{\downarrow} are the eigenvalues of $\rho(t)$ arranged in nonincreasing order and $|\varepsilon_k^{\uparrow}\rangle$ are the eigenstates of H_B ordered by increasing eigenvalues E_k .

In our model, the battery Hamiltonian coincides with the Hermitian SSH Hamiltonian H_{SSH} introduced in Sec. II A, and its eigenstates are denoted by $\{|\phi_j\rangle\}$ with eigenvalues $\{E_j\}$ ordered such that $E_1 \leq \dots \leq E_{2N}$. The ground state of the battery is therefore $|G\rangle = |\phi_1\rangle$, and the initial state is prepared as the corresponding projector,

$$\rho(0) = |G\rangle \langle G| = |\phi_1\rangle \langle \phi_1|, \quad (\text{C3})$$

which represents a pure state with minimum energy

$$E_B(0) = \langle G | H_B | G \rangle = E_1. \quad (\text{C4})$$

During the non-Hermitian charging process, the battery evolves according to the normalized effective dynamics defined in Eq. (8). Since this map is generated by $H_{\mathcal{PT}}$ acting on a pure initial state and involves a renormalization at each time step, the density matrix remains pure for all t ,

$$\rho(t) = |\psi(t)\rangle \langle \psi(t)|. \quad (\text{C5})$$

Hence, the spectrum of $\rho(t)$ contains a single nonzero eigenvalue equal to one, independently of the detailed superposition $|\psi(t)\rangle$.

Because the passive state is obtained by rearranging the eigenvalues of $\rho(t)$ in a basis that minimizes the energy, and there is only one nonzero eigenvalue, the passive counterpart of $\rho(t)$ is simply the ground-state projector,

$$\rho_{\text{p}} = |G\rangle \langle G| = |\phi_1\rangle \langle \phi_1|. \quad (\text{C6})$$

Substituting this ρ_p into Eq. (C1) yields

$$\begin{aligned}\mathcal{W}(t) &= \text{Tr}[H_B \rho(t)] - \text{Tr}[H_B |G\rangle\langle G|] \\ &= E_B(t) - E_B(0) \\ &\equiv \Delta E(t),\end{aligned}\quad (\text{C7})$$

where $E_B(t) = \text{Tr}[H_B \rho(t)]$ is the instantaneous energy of the battery. Therefore, for a pure initial state undergoing the normalized non-Hermitian evolution of Eq. (8) under $H_{\mathcal{PT}}$, the ergotropy is exactly equal to the charging energy,

$$\mathcal{W}(t) = \Delta E(t). \quad (\text{C8})$$

This result implies that, within the no-jump effective description adopted in the main text, the stored energy $\Delta E(t)$ alone faithfully characterizes the extractable work of the \mathcal{PT} -symmetric SSH quantum battery.

Appendix D: Universal principles of non-Hermitian dynamics

In this appendix, we summarize three general principles that govern the time evolution of diagonalizable non-Hermitian systems. These principles follow directly from the spectral decomposition of the evolution operator and are independent of the microscopic details of the Hamiltonian.

We consider a non-Hermitian Hamiltonian H with right eigenvectors $|\phi_j\rangle$ and complex eigenvalues $E_j = \omega_j + i\lambda_j$, where ω_j and λ_j denote the real and imaginary parts, respectively. We assume that H is diagonalizable, i.e., that the system is not tuned exactly to an exceptional point, so that the set $\{|\phi_j\rangle\}$ spans the Hilbert space. Starting from an initial state $|\psi(0)\rangle = \sum_j a_j |\phi_j\rangle$, the unnormalized state evolves as

$$|\psi_{\text{un}}(t)\rangle = e^{-iHt} |\psi(0)\rangle = \sum_j a_j e^{-iE_j t} |\phi_j\rangle. \quad (\text{D1})$$

In many applications, including the main text, one works with the normalized state

$$|\psi(t)\rangle = \frac{|\psi_{\text{un}}(t)\rangle}{\|\psi_{\text{un}}(t)\rangle}, \quad (\text{D2})$$

or with the corresponding density matrix $\rho(t) = |\psi(t)\rangle\langle\psi(t)|$.

The *long-time behavior* is governed solely by the imaginary parts $\{\lambda_j\}$. Let $\lambda_{\max} = \max_j \lambda_j$ be the largest growth rate and assume it is nondegenerate. Then, for $t \rightarrow \infty$, the contribution of the eigenmode with λ_{\max} dominates $|\psi_{\text{un}}(t)\rangle$, and after normalization the state converges to the corresponding eigenvector,

$$|\psi(t)\rangle \xrightarrow[t \rightarrow \infty]{} |\phi_{\max}\rangle, \quad (\text{D3})$$

where $|\phi_{\max}\rangle$ is the eigenstate with $\text{Im } E_{\max} = \lambda_{\max}$. If several modes share the same maximal imaginary part, the long-time state resides in the subspace spanned by these modes, but the final superposition is determined by the initial coefficients $\{a_j\}$.

The *relaxation timescale* is set by the gap between the leading growth rates. Denoting by λ_2 the second-largest imaginary part, the difference

$$\Delta\lambda = \lambda_{\max} - \lambda_2 \quad (\text{D4})$$

controls how quickly the dominant mode overwhelms its competitors. A larger gap $\Delta\lambda$ leads to rapid convergence to the asymptotic state, while nearly degenerate growth rates produce a prolonged competition among several modes. This observation underlies the estimate

$$\tau^{-1} \sim \lambda_{\max} - \lambda_2, \quad (\text{D5})$$

used in the main text to relate spectral properties to charging times.

At *early times*, however, the dynamics is controlled primarily by the initial projections a_j rather than by the growth rates. Modes with large initial overlap can dominate the short-time evolution even if they do not possess the largest imaginary parts. As time increases, the exponential factors $e^{\lambda_j t}$ eventually amplify the contribution of the leading mode(s), and the role of the initial coefficients becomes subdominant.

These three ingredients—initial overlaps, the gap between the leading imaginary parts, and the identity of the mode(s) with maximal λ_j —provide a universal framework for analyzing non-Hermitian dynamics. They explain in a model-independent way the transient and asymptotic features of the population dynamics discussed in Sec. III C, including the dominance of the extremal SSH eigenpair at weak non-Hermiticity, the edge-assisted acceleration of saturation in the topological phase, and the late-time selection of band-center modes in the fully broken regime.

[1] F. Campaioli, S. Gherardini, J. Q. Quach, M. Polini, and G. M. Andolina, *Colloquium : Quantum batteries*, *Rev. Mod. Phys.* **96**, 031001 (2024).

[2] S. Pokhrel and J. Gea-Banacloche, Large Collective Power Enhancement in Dissipative Charging of a Quantum Battery, *Phys. Rev. Lett.* **134**, 130401 (2025).

[3] R. P. A. Simon, J. Anders, and K. V. Hovhannisyan, Correlations Enable Lossless Ergotropy Transport, *Phys. Rev. Lett.* **134**, 010408 (2025).

[4] J.-Y. Gyhm and U. R. Fischer, Beneficial and detrimental entanglement for quantum battery charging, *AVS Quantum Science* **6**, 012001 (2024).

[5] F. Mayo and A. J. Roncaglia, Collective effects and quantum coherence in dissipative charging of quantum batteries, *Phys. Rev. A* **105**, 062203 (2022).

[6] Y. F. Li, S. R. He, P. H. Ouyang, X. N. Feng, and L. F. Wei, Switchable coherent quantum batteries with large ergotropy, *Phys. Rev. A* **112**, 022217 (2025).

[7] H.-L. Shi, S. Ding, Q.-K. Wan, X.-H. Wang, and W.-L. Yang, Entanglement, Coherence, and Extractable Work in Quantum Batteries, *Phys. Rev. Lett.* **129**, 130602 (2022).

[8] R. Alicki and M. Fannes, Entanglement boost for extractable work from ensembles of quantum batteries, *Phys. Rev. E* **87**, 042123 (2013).

[9] F. Campaioli, F. A. Pollock, F. C. Binder, L. Céleri, J. Goold, S. Vinjanampathy, and K. Modi, Enhancing the charging power of quantum batteries, *Phys. Rev. Lett.* **118**, 150601 (2017).

[10] D. Ferraro, M. Campisi, G. M. Andolina, V. Pellegrini, and M. Polini, High-Power Collective Charging of a Solid-State Quantum Battery, *Phys. Rev. Lett.* **120**, 117702 (2018).

[11] S. S. Seidov and S. I. Mukhin, Quantum Dicke battery supercharging in the bound-luminosity state, *Phys. Rev. A* **109**, 022210 (2024).

[12] L. Fusco, M. Paternostro, and G. De Chiara, Work extraction and energy storage in the dicke model, *Phys. Rev. E* **94**, 052122 (2016).

[13] F.-Q. Dou, Y.-Q. Lu, Y.-J. Wang, and J.-A. Sun, Extended dicke quantum battery with interatomic interactions and driving field, *Phys. Rev. B* **105**, 115405 (2022).

[14] A. Crescente, M. Carrega, M. Sassetti, and D. Ferraro, Ultrafast charging in a two-photon Dicke quantum battery, *Phys. Rev. B* **102**, 245407 (2020).

[15] G. M. Andolina, M. Keck, A. Mari, V. Giovannetti, and M. Polini, Quantum versus classical many-body batteries, *Phys. Rev. B* **99**, 205437 (2019).

[16] S. Ghosh, T. Chanda, and A. Sen(De), Enhancement in the performance of a quantum battery by ordered and disordered interactions, *Phys. Rev. A* **101**, 032115 (2020).

[17] Y. Su, W. Lu, and H.-L. Shi, Quantum metrology enhanced by the xy spin interaction in a generalized tavis-cummings model, *Phys. Rev. A* **109**, 042614 (2024).

[18] F.-Q. Dou, M.-P. Han, and C.-C. Shu, Quantum speed limit under brachistochrone evolution, *Phys. Rev. Appl.* **20**, 014031 (2023).

[19] M. Z. Hasan and C. L. Kane, Colloquium: Topological insulators, *Rev. Mod. Phys.* **82**, 3045 (2010).

[20] J. K. Asbóth, L. Oroszlány, and A. Pályi, *A Short Course on Topological Insulators*, Lecture Notes in Physics, Vol. 919 (Springer International Publishing, Cham, 2016).

[21] W. P. Su, J. R. Schrieffer, and A. J. Heeger, Solitons in Polyacetylene, *Phys. Rev. Lett.* **42**, 1698 (1979).

[22] F. Zhao, F.-Q. Dou, and Q. Zhao, Charging performance of the Su-Schrieffer-Heeger quantum battery, *Phys. Rev. Research* **4**, 013172 (2022).

[23] Z.-G. Lu, G. Tian, X.-Y. Lü, and C. Shang, Topological Quantum Batteries, *Phys. Rev. Lett.* **134**, 180401 (2025).

[24] Y. Guo, L. Cao, and J. Zhao, Nonreciprocal open quantum battery network in a photonic waveguide array, *Phys. Rev. A* **111**, 063520 (2025).

[25] J. Carrasco, J. R. Maze, C. Hermann-Avigliano, and F. Barra, Collective enhancement in dissipative quantum batteries, *Phys. Rev. E* **105**, 064119 (2022).

[26] C.-Y. Zhang and J. Jing, Dissipative qutrit-mediated stable charging, *Phys. Rev. A* **112**, 032206 (2025).

[27] F. Zhao, F.-Q. Dou, and Q. Zhao, Quantum battery of interacting spins with environmental noise, *Phys. Rev. A* **103**, 033715 (2021).

[28] S. Ghosh, T. Chanda, S. Mal, and A. Sen(De), Fast charging of a quantum battery assisted by noise, *Phys. Rev. A* **104**, 032207 (2021).

[29] J. Q. Quach and W. J. Munro, Using Dark States to Charge and Stabilize Open Quantum Batteries, *Phys. Rev. Applied* **14**, 024092 (2020).

[30] K. V. Hovhannisyan, F. Barra, and A. Imparato, Charging assisted by thermalization, *Phys. Rev. Research* **2**, 033413 (2020).

[31] D. Manzano, A short introduction to the Lindblad master equation, *AIP Advances* **10**, 025106 (2020).

[32] K. Wilma, C.-C. Shu, U. Scherf, and R. Hildner, Visualizing hidden ultrafast processes in individual molecules by single-pulse coherent control, *Journal of the American Chemical Society* **140**, 15329 (2018).

[33] R. El-Ganainy, K. G. Makris, M. Khajavikhan, Z. H. Musslimani, S. Rotter, and D. N. Christodoulides, Non-hermitian physics and PT symmetry, *Nature Physics* **14**, 11 (2018).

[34] Y. Ashida, Z. Gong, and M. Ueda, Non-hermitian physics, *Adv. Phys.* **69**, 249 (2020).

[35] H. Li, J.-K. Shi, L.-B. Fan, Z.-M. Li, and C.-C. Shu, Anisotropic Rabi model with two-photon relaxation, *Phys. Rev. A* **110**, 023708 (2024).

[36] T. K. Konar, L. G. C. Lakkaraju, and A. Sen (De), Quantum battery with non-Hermitian charging, *Phys. Rev. A* **109**, 042207 (2024).

[37] C. M. Bender, Introduction to PT-symmetric quantum theory, *Contemp. Phys.* **46**, 277 (2005).

[38] S. Dogra, A. A. Melnikov, and G. S. Paraoanu, Quantum simulation of parity-time symmetry breaking with a superconducting quantum processor, *Commun. Phys.* **4**, 26 (2021).

[39] M. Klett, H. Cartarius, D. Dast, J. Main, and G. Wunner, Relation between PT -symmetry breaking and topologically nontrivial phases in the Su-Schrieffer-Heeger and Kitaev models, *Phys. Rev. A* **95**, 053626 (2017).

[40] B. Zhu, R. Lü, and S. Chen, PT symmetry in the non-Hermitian Su-Schrieffer-Heeger model with complex boundary potentials, *Phys. Rev. A* **89**, 062102 (2014).

[41] S. K. Özdemir, S. Rotter, F. Nori, and L. Yang, Parity-time symmetry and exceptional points in photonics, *Nat. Mater.* **18**, 783 (2019).

[42] J. M. Zeuner, M. C. Rechtsman, Y. Plotnik, Y. Lumer, S. Nolte, M. S. Rudner, M. Segev, and A. Szameit, Observation of a topological transition in the bulk of a non-hermitian system, *Phys. Rev. Lett.* **115**, 040402 (2015).

[43] D. Braak, Integrability of the Rabi model, *Phys. Rev. Lett.* **107**, 100401 (2011).

[44] Z.-M. Li and M. T. Batchelor, Hidden symmetry and tunneling dynamics in asymmetric quantum Rabi models, *Phys. Rev. A* **103**, 023719 (2021).

[45] Z.-M. Li and M. T. Batchelor, Generalized adiabatic approximation to the quantum Rabi model, *Phys. Rev. A* **104**, 033712 (2021).

[46] Q. Xie, H. Zhong, M. T. Batchelor, and C. Lee, The quantum Rabi model: Solution and dynamics, *J. Phys. A: Math. Theor.* **50**, 113001 (2017).

[47] Z.-M. Li and M. T. Batchelor, Algebraic equations for the exceptional eigenspectrum of the generalized Rabi model, *J. Phys. A: Math. Theor.* **48**, 454005 (2015).

[48] Q.-T. Xie, S. Cui, J.-P. Cao, L. Amico, and H. Fan, Anisotropic Rabi model, *Phys. Rev. X* **4**, 021046 (2014).

[49] X. Lu, H. Li, J.-K. Shi, L.-B. Fan, V. Mangazeev, Z.-M. Li, and M. T. Batchelor, PT-symmetric quantum Rabi model, *Phys. Rev. A* **108**, 053712 (2023).

[50] L.-B. Fan, C.-C. Shu, D. Dong, J. He, N. E. Henriksen, and F. Nori, Quantum Coherent Control of a Single Molecular-Polariton Rotation, *Phys. Rev. Lett.* **130**, 043604 (2023).

[51] A. F. Tzortzakakis, A. Katsaris, N. E. Palaiodimopoulos, P. A. Kalozoumis, G. Theocharis, F. K. Diakonos, and D. Petrosyan, Topological edge states of the \mathcal{PT} -symmetric su-schrieffer-heeger model: An effective two-state description, *Phys. Rev. A* **106**, 023513 (2022).

[52] T. K. Konar, L. G. C. Lakkaraju, S. Ghosh, and A. Sen(De), Quantum battery with ultracold atoms: Bosons versus fermions, *Phys. Rev. A* **106**, 022618 (2022).

[53] S. Ghosh and A. Sen(De), Dimensional enhancements in a quantum battery with imperfections, *Phys. Rev. A* **105**, 022628 (2022).

[54] D. Dast, D. Haag, H. Cartarius, and G. Wunner, Quantum master equation with balanced gain and loss, *Phys. Rev. A* **90**, 052120 (2014).

[55] Y. Nakanishi and T. Sasamoto, PT phase transition in open quantum systems with Lindblad dynamics, *Phys. Rev. A* **105**, 022219 (2022).

[56] B. He, S.-B. Yan, J. Wang, and M. Xiao, Quantum noise effects with Kerr-nonlinearity enhancement in coupled gain-loss waveguides, *Phys. Rev. A* **91**, 053832 (2015).

[57] J. Huber, P. Kirton, S. Rotter, and P. Rabl, Emergence of PT-symmetry breaking in open quantum systems, *SciPost Phys.* **9**, 052 (2020).

[58] F. Mei, G. Chen, L. Tian, S.-L. Zhu, and S. Jia, Robust quantum state transfer via topological edge states in superconducting qubit chains, *Phys. Rev. A* **98**, 012331 (2018).

[59] S. Lin, L. Zhang, T. Tian, C.-K. Duan, and J. Du, Dynamic observation of topological soliton states in a programmable nanomechanical lattice, *Nano Letters* **21**, 1025 (2021).

[60] A. E. Allahverdyan, R. Balian, and T. M. Nieuwenhuizen, Maximal work extraction from finite quantum systems, *Europhys. Lett.* **67**, 565 (2004).

[61] X. Yang, Y.-H. Yang, M. Alimuddin, R. Salvia, S.-M. Fei, L.-M. Zhao, S. Nimmrichter, and M.-X. Luo, Battery capacity of energy-storing quantum systems, *Phys. Rev. Lett.* **131**, 030402 (2023).